ROYAL SOCIETY
OF CHEMISTRY

PAPER

Check for updates

Facile synthesis of mesoporous $Ni_xCo_{9-x}S_8$ hollow spheres for high-performance supercapacitors and aqueous Ni/Co–Zn batteries†

Daojun Zhang, [ID] * Jingchao Zhang, Jiaqi Li, Chengxiang Li, Yuting Li, Yingying Liu and Renchun Zhang

Porous micro/nanostructure electrode materials have always contributed to outstanding electrochemical energy storage performances. Co_9S_8 is an ideal model electrode material with high theoretical specific capacity due to its intrinsic two crystallographic sites of cobalt ions. In order to improve the conductivity and specific capacitance of Co_9S_8, nickel ions were introduced to tune the electronic structure of Co_9S_8. The morphology design of the mesoporous hollow sphere structure guarantees cycle stability and ion diffusion. In this work, $Ni_xCo_{9-x}S_8$ mesoporous hollow spheres were synthesized *via* a facile partial ion-exchange of Co_9S_8 mesoporous hollow spheres without using a template, boosting the capacitance to 1300 F g^{-1} at the current density of 1 A g^{-1}. Compared with the pure Co_9S_8 and Ni-Co_9S_8-30%, Ni-Co_9S_8-60% exhibited the best supercapacitor performance, which was ascribed to the maximum Ni ion doping with morphology and structure retention, enhanced conductivity and stabilization of Co^{3+} in the structure. Therefore, Ni/Co–Zn batteries were fabricated by using a Zn plate as the anode and Ni-Co_9S_8-60% as the cathode, which deliver a high energy density of 256.5 W h kg^{-1} at the power density of 1.69 kW kg^{-1}. Furthermore, the Ni/Co–Zn batteries exhibit a stable cycling after 3000 repeated cycles with capacitance retention of 69% at 4 A g^{-1}. This encouraging result might provide a new perspective to optimize Co_9S_8-based electrodes with superior supercapacitor and Ni/Co–Zn battery performances.

1 Introduction

In recent years, as an important transition metal sulfide, Co_9S_8 has been regarded as one of the most attractive electrode materials with a high theoretical specific capacity (5449 F g^{-1} at 0.45 V),[1] low cost and non-toxic nature, however, the presence of sluggish ion transport kinetics and low conductivity limits its application in the energy storage field. Thus a lot of efforts have been devoted to improving the conductivity by conductive metals or carbonaceous supports,[2–6] ion-doping,[7] constructing hierarchical composites,[8] graphene hybridization,[9,10] carbon coating,[11] and constructing hetero-phase interfaces.[12–14] In addition to consideration of the conductivity, the electrochemical performance is also dependent on the accessible surface area of transition metal based micro/nanomaterials,[15–17] thus a lot of effect has been devoted to synthesizing electrode materials with large surface areas and porous structures. For

example, the reported morphology and synthesis strategies include ion exchange reaction,[6] microwave irradiation,[18] sacrificial metal salt hard templates[19] and derivation from metal–organic framework precursors *via* a sulfuration process.[20,21] Considering the complexity and multiple steps of the template transformation method, it is worth developing a simple method without a template to obtain hollow sphere structures.

In general, the mesoporous hollow structure can alleviate the volumetric expansion, accommodate large internal and external surface area and facile electrolyte ions diffusion reaction.[22–24] For example, Zheng reported the metallic hollow Co_9S_8 sphere can serve as sulfur hosts in Li–S batteries and promote interfacial redox reaction kinetics, which present excellent rate performance and high stability.[25] Feng designed hierarchical Co_9S_8@carbon hollow microspheres *via* a solvothermal reaction and subsequent annealing process, which also exhibited remarkable sodium storage performance with remarkable cycling stability.[26] Li reported the synthesis of hollow spherical Co_9S_8 using presynthetic silica hollow spheres template to construct Co–SiO_2 precursor and subsequent hydrothermal sulfurizing process.[27] Guo *et al.* using bacteria as template *via* hydrothermal and further calcination process to fabricate porous Co_9S_8/CoS/C submicronspheres.[28] Thus a facile one-step method to prepare Co_9S_8 porous spheres especially mesoporous hollow architecture is appreciated.

College of Chemistry and Chemical Engineering, Anyang Normal University, Anyang, 455000, Henan, China. E-mail: zhangdj0410@126.com; zhangdj0410@sohu.com; Tel: +86 372 2900040

Transition metal sulfides especially porous hollow structures are considered as promising electrode materials for electrochemical energy storage devices (EESDs) owing to their relatively abundant, low cost, non-toxic nature, multiple electrochemical reaction sites with high capacity.[29,30] Alkaline aqueous EESDs, such as supercapacitor and Ni/Co–Zn batteries, have many merits consist of environmental friendliness and quickly charge–discharge speed attribute to using high ionic conductance of OH^- anions as the charge carries, thus alkaline aqueous EESDs have great potential applications in energy storage field.[31,32] Especially, Co-based sulfides were considered to be good cathodes with high theoretical capacity and operating voltage, which attracted extensive research interests.[33] Extensive exploring micro/nanostructure is help to increase the capacity output and rate capability of cathode.[34] The structure of Co_9S_8 is a typical structure with the octahedral site of Co^{3+} and tetrahedral site of Co^{2+}. Therefore, doping Ni ions into Co_9S_8 is a promising strategy to increase the Co^{3+} and Ni^{3+} content in the octahedral sites of Co_9S_8 lattices, which effectively synergistic increase the capacity and cycling stability of supercapacitor and Co–Ni//Zn battery. Nevertheless, the investigation of $Ni_xCo_{9-x}S_8$ as cathode material in alkaline Ni–Zn battery is rarely reported till now.

Herein, a facile cation exchange approach to synthesize mesoporous hollow structured $Ni_xCo_{9-x}S_8$ using the solvothermal synthesized Co_9S_8 microspheres as precursors. The nickel ion doping improves the conductivity of parent Co_9S_8 and promotes electrochemical reaction kinetics. The Ni-Co_9S_8-0.6 shows a battery-type faradaic electrode, which can offer additional charge storage capacity *via* surface redox processes, *e.g.*, 1300 F g^{-1} at 1 A g^{-1}, compared with the pure Co_9S_8 electrode (430 F g^{-1} at 1 A g^{-1}). Furthermore, we exhibit a novel Ni/Co–Zn battery utilizing Ni-Co_9S_8-0.6 mesoporous hollow microspheres as cathode material, due to the high content Co^{3+} ions of Ni-Co_9S_8-0.6, the voltage window of Ni/Co–Zn battery can achieve 1.93 V *vs.* Zn. These special designs are helped to improve the kinetic property and rate property of the cathode material. This new Ni/Co–Zn battery shows a high power density of 1.69 kW kg^{-1} at the energy density of 256.46 W h kg^{-1}.

2 Experimental

2.1 Preparation of $Ni_xCo_{9-x}S_8$ mesoporous hollow microspheres

To prepare Co_9S_8 microspheres, 0.1 mmol of cobalt acetate tetrahydrate was dissolved in a mixture solution of *N,N*-dimethylformamide (4 mL), tetramethyl-ethylenediamine (3 mL), and ethanolamine (1 mL) under strong stirring for 0.5 h. Afterwards, 0.1 mmol of thioacetamide was added and further stirred for another 0.5 h. Then the solution was transferred to a 20 mL autoclave and heated at 180 °C for 12 h. The black precipitate was collected by centrifugation and dried at 60 °C for 30 min.

For the synthesis of Ni-Co_9S_8-30% and Ni-Co_9S_8-60% microspheres, the equal amounts (0.03/0.06 mmol) of nickel acetate and thiourea was added to the pre-dispersed aqueous solution (6 mL) containing the as-prepared Co_9S_8 microspheres,

then 2 mL of ethylene glycol were added with vigorous stirring, subsequently heated to 160 °C and kept for 4 h. The final samples were washed and dried in vacuum at 60 °C for 30 min. Herein, we use Ni-Co_9S_8-0.3 and Ni-Co_9S_8-0.6 to denote the 30% and 60% Ni ions added in the reaction system.

2.2 Material characterization

The resultant phase of the mesoporous Co_9S_8, Ni-Co_9S_8-0.3 and Ni-Co_9S_8-0.6 hollow microspheres was determined by X-ray diffraction (XRD) on a PANalytical X' Pert operated at 40 kV and 40 mA. The morphology and microstructure were studied by SEM and TEM technique. The composition and chemical states of the samples was further analyzed by energy-dispersive X-ray spectroscopy (EDS) as well as X-ray photoelectron spectroscopy (XPS, ESCALab, 250XI), respectively. The specific surface area of the samples was measured by N_2 adsorption analyzer (Gemini VII 2390).

2.3 Cathode electrode preparation and measurement

For preparation supercapacitor and alkaline Ni–Zn battery cathode, the electrode slurry was prepared by mixing 16 mg of the $Ni_xCo_{9-x}S_8$ powders, 2 mg of acetylene black, and 2 mg of polyvinylidene-fluoride with 110 μL of *N*-methylpyrrolidone. Then, the slurry was carefully coated onto the pretreated Ni foam with the area of 1 cm × 1 cm, and dried in vacuum at 80 °C for 10 h. The specific capacitance C_s of supercapacitor was calculated from following equation:

$$C_s = \frac{I \times \Delta t}{m \times \Delta V}$$

where I, Δt, m, ΔV is the current density, discharge time, the mass of active materials, and the potential window, respectively.

The alkaline Ni–Zn battery tests were recorded on an electrochemical workstation (CHI 660E) using two electrode system in which Zn plate as reference and counter electrode, and Ni-Co_9S_8-0.6 as working electrode, 2 M KOH and 20 mM Zn(Ac)$_2$ were used as mixture electrolytes. AC impendence tests with a platinum coil counter electrode and a saturated calomel electrode as reference electrode. The electrochemical impendence plots were collected at open circuit potential at the frequency range of 0.01 Hz–1 MHz.

3 Results and discussion

Scheme 1 shows the one-step synthesis of unique mesoporous Co_9S_8 hollow microspheres *via* a mixed solvothermal route, then Ni-doped Co_9S_8 can be obtained by a cation-exchange method with introducing 0.03 or 0.06 mmol nickel acetate and thiourea in a water–ethylene glycol system. Herein, we use Ni-Co_9S_8-0.3 and Ni-Co_9S_8-0.6 to denote the 30% and 60% Ni ions added in the reaction system, and aim to investigate the role of Ni doping in promoting the supercapacitor properties of Co_9S_8 particles.

The morphology and composition of Co_9S_8 mesoporous hollow spheres were characterized by SEM and EDS. Fig. S1a† and 1a show SEM images of the as-prepared Co_9S_8
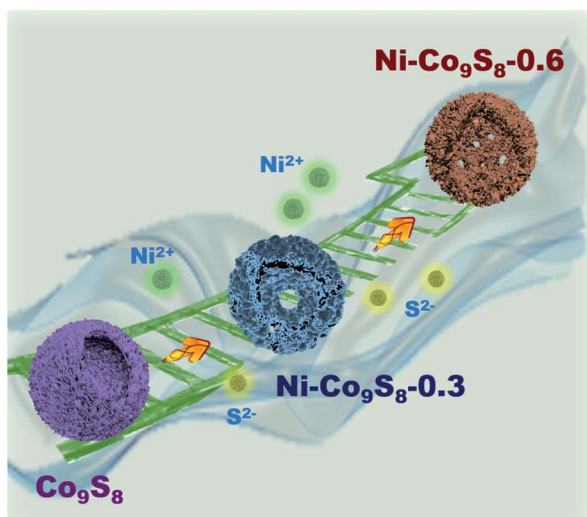
Scheme 1 The synthesis procedure of $Ni_xCo_{9-x}S_8$ series hollow spheres.

microspheres at low and high magnification, it is clearly seen that microspheres assembled by numerous interconnected nanosheets with large inner cavity, after introducing Ni ions,
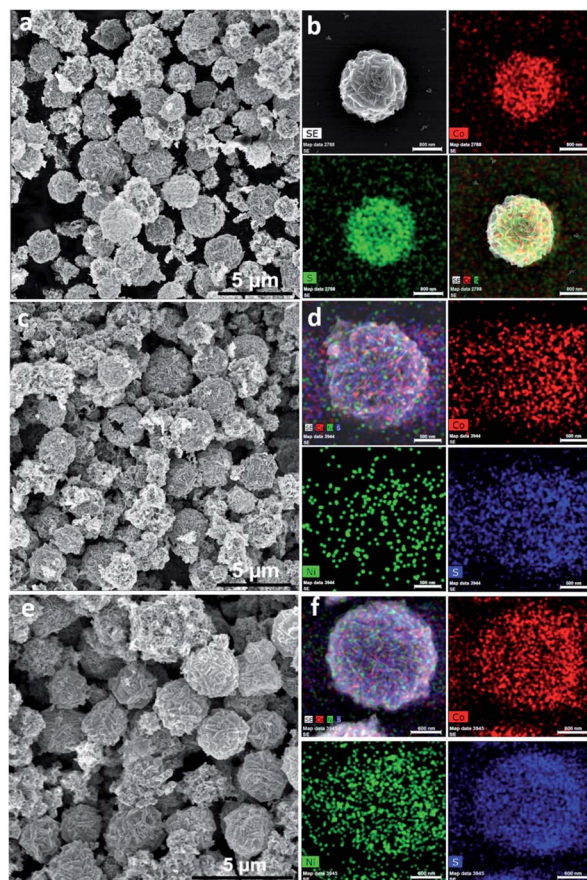

Fig. 1 SEM images and EDS element mapping of (a and b) Co_9S_8, (c and d) $Ni-Co_9S_8$-0.3, (e and f) $Ni-Co_9S_8$-0.6 hollow microspheres. (The scale bar of b, d, f is 800, 500 and 600 nm).
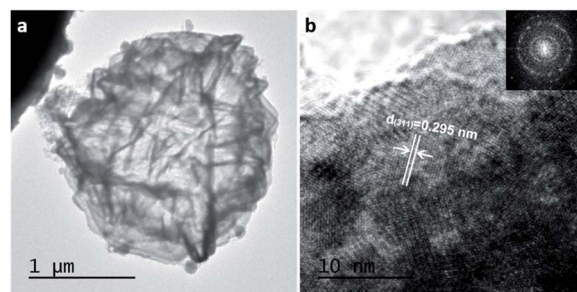

Fig. 2 TEM images of $Ni-Co_9S_8$-0.6 hollow spheres. (a) A single $Ni-Co_9S_8$-0.6 hollow sphere, (b) HRTEM image.

the hollow sphere morphology can be well preserved with thinner size and more closely stacked nanosheets. The as-prepared Co_9S_8 microspheres exhibited an average diameter of ∼2.65 μm (Fig. S1b†). The cracked microspheres provide insights into the hollow interior and the assembly structure. After the Ni ions doping, the microsphere size decreases to from 2.34 to 2.29 μm (Fig. 1c, e, and S1†), which may due to the breakage of the big microspheres *via* the second step of Ni ions exchange. As shown in the EDS element mapping (Fig. 1d), the cobalt and sulfur elements are homogenous distributed in the Co_9S_8 microspheres. The intensity of Ni element mapping raised following the increase of Ni content in Co_9S_8 matrics (Fig. 1d and f).

The TEM image of a typical $Ni-Co_9S_8$-0.6 hollow microsphere was shown in Fig. 2a, which shows a sharp contrast between the inner cavity and cross stacking nanosheets shell. The special microstructure not only avoid the aggregation and structural collapse, but also provide more surface and inner exposed active sites, which help to achieve desirable rate and cycling performance due to the fast ion diffusion. The lattice interplanar spacing measured to be ∼0.295 nm, which matched well with the (311) plane of cobalt pentlandite Co_9S_8 (Fig. 2b), indicating the structure of Co_9S_8 was stable in moderate Ni ions doping.
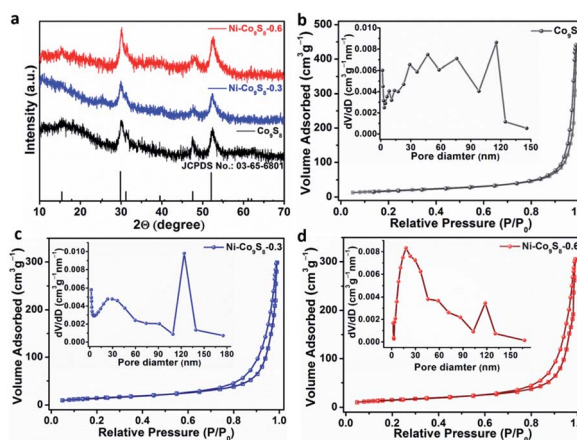

Fig. 3 (a) XRD patterns of $Ni_xCo_{9-x}S_8$ series hollow spheres. Nitrogen adsorption−desorption isotherms and the corresponding pore size distributions (inset) of (b) Co_9S_8, (c) $Ni-Co_9S_8$-0.3, and (d) $Ni-Co_9S_8$-0.6 hollow spheres.

The phase purities of as-synthesized microspheres were further detected by X-ray power diffraction (Fig. 3a), the diffraction peaks of the three samples match well with the cubic Co_9S_8 phase. The XRD patterns of the three samples are similar, for example, the obtained XRD of Co_9S_8 mesoporous microspheres shown three obvious diffraction peaks at ~29.8, 47.5 and 52.1°, which corresponded to the (311), (511), and (400) plane of Co_9S_8 (JCPDS no: 03-65-6801). Because the Co ion radius is larger than the Ni ion, the diffraction peaks of Ni ions doped microspheres especially Ni-Co_9S_8-0.6 present a slight moving to higher angle of 2 Theta than pure Co_9S_8, and the calculated d-spacing of (311) plane from Scherrer formula is 0.296 nm, which is lower than that of pure Co_9S_8 (0.299 nm). The XRD result is almost consistent with the HRTEM in Fig. 2b. The energy-dispersive X-ray spectroscopy (EDS) results indicated the presence of Co, S and Ni elements in the series samples. The ratio of Co/S in Co_9S_8 is 9 : 8, which is consistent with the stoichiometry of Co_9S_8. The Ni/Co/S ratio of Ni-Co_9S_8-0.3 and Ni-Co_9S_8-0.6 samples is 1.4 : 7.6 : 6 and 2.8 : 6.2 : 6.5, respectively (Fig. S2†). Therefore, both XRD and EDS results confirmed the pure phase of the Ni doped series of $Ni_xCo_{9-x}S_8$. To analyse the surface area and porous structure of the series of hollow spheres, N_2 adsorption–desorption isotherms were conducted. The hysteresis loop for Co_9S_8 located above $P/P_0 = 0.8$, indicating the presence of mesoporous structure (Fig. 3b). The inset is the Barrett–Joyner–Halenda (BJH) pore distribution for pure Co_9S_8, the mean pore size is ~47 nm with the BET surface area of 65.92 m^2 g^{-1}. The surface area of Co_9S_8 (65.92 m^2 g^{-1}) is larger than Ni-Co_9S_8-0.3 (54.18 m^2 g^{-1}) and Ni-Co_9S_8-0.6 (55.73 m^2 g^{-1}) samples as shown in Fig. 3c and d. In addition, the mean pore distribution for Ni-Co_9S_8-0.3 and Ni-Co_9S_8-0.6 decreased to 29.21 and 18.08 nm after nickel ions exchange into Co_9S_8 structure. Thus, the porous structure facilitates electrolyte diffusion and electron transport during the redox electrochemical reaction.

Furthermore, XPS in Fig. 4 also indicated the existence of Co, S, and Ni elements in the as-obtained Ni-Co_9S_8-0.3 and Ni-

Co_9S_8-0.6 microspheres and the variation of surface chemical state of Co after Ni ion doping. In the Co 2p spectra of pure Co_9S_8 and Ni-doped Co_9S_8 indicated the presence of Co^{2+} and Co^{3+} in the tetrahedral and octahedral sites. The peaks at ~778.34 and 793.42 eV for Co_9S_8 were ascribed to Co^{3+}, while those at 780.81 and 796.62 eV belonged to Co^{2+}.[35] It can be seen from Fig. 4b that the Co^{3+} area of Ni-Co_9S_8-0.6 is higher than Co_9S_8, the ratio of Co^{3+}/Co^{2+} obtained from their respective main lines is 0.3529 for Ni-Co_9S_8-0.6 and 0.3248 for Co_9S_8. The peaks located at 712.40 and 724.30 eV, with the satellite of 718.60 and 736.41 eV, indicated the existence of Ni^{3+}, which caused the increase of Co^{3+}/Co^{2+} ratio in Ni-Co_9S_8-0.6 microspheres. Meanwhile, the Ni^{3+}/Ni^{2+} ratio of is 1.88 for Ni-Co_9S_8-0.3 and 2.38 for Ni-Co_9S_8-0.6 (Table S1†). Thus, we conclude that the nickel ions doping supply more trivalent sites in Co_9S_8 structure, which is helped to regulate cationic distribution and increase the output voltage of the electrode materials. The typical binding energy peaks S $2p_{3/2}$ and S $2p_{1/2}$ were located at 161.46 and 162.68 eV, respectively, the peak located at 59.60 eV may be ascribed to a small degree of surface oxidation of the catalyst exposed to the air condition.

3.1 Electrochemical performance of mesoporous $Ni_xCo_{9-x}S_8$ hollow microspheres

To evaluate the supercapacitance performance of the series $Ni_xCo_{9-x}S_8$ samples, electrochemical tests were conducted by a standard three-electrode system in 2.0 M KOH aqueous solution, with sample coated Ni foam as work electrode, Hg/Hg_2Cl_2 and Pt plate as reference electrode and counter electrode. The CV curves of the Co_9S_8, Ni-Co_9S_8-0.3, and Ni-Co_9S_8-0.6 electrodes were plotted in Fig. 5a, S3 and S4.† Co_9S_8 sample present two pairs of redox peaks in the CV curve, which can be attributed to the redox reaction of Co_9S_8 with two Co crystallographic sites in its structure. Compared with the Co^{2+}/Co^{3+} and Co^{3+}/Co^{4+} redox peaks of Co_9S_8 electrode, the Ni doped Co_9S_8 exhibited an obvious increase of peak intensity and increased integration area because of the coexistence of Ni^{2+}/Ni^{3+}, indicated the better performance of the Ni-doped samples. Fig. 5b indicated the intercalation and surface reaction mechanism occurred in the series of $Ni_xCo_{9-x}S_8$ electrodes. The corresponding diffusion contribution of Co_9S_8, Ni-Co_9S_8-0.3 and Ni-Co_9S_8-0.6 is 48%, 56%, and 61%, respectively, demonstrating the diffusion-controlled behavior at 5 mV s^{-1}. Conversely, with the increase of scan rate, the capacitive contribution enhanced due to the insufficient time for intercalation reaction into the series of $Ni_xCo_{9-x}S_8$ electrodes. The galvanostatic charge–discharge (GCD) plot of the three electrodes was shown in Fig. 5c and S5.† At a current density of 1 A g^{-1}, the Ni-Co_9S_8-0.6 electrode exhibits the longest discharge time, furthermore, according to the galvanostatic discharge curves, the calculated capacitances of Ni-Co_9S_8-0.6, Ni-Co_9S_8-0.3, and Co_9S_8 electrodes are 1300, 653, and 430 F g^{-1}, respectively. As the current density increase to 10 A g^{-1}, the corresponding capacitance decreased to 1048, 536, and 346 F g^{-1} (Fig. 5d), and the corresponding capacitance retentions are 80.6%, 82.1%, and 80.5%, respectively. The above results indicated the introducing of Ni ions
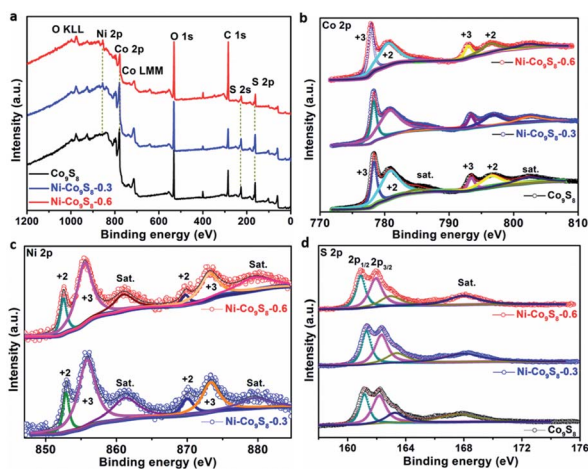

Fig. 4 (a) XPS survey of $Ni_xCo_{9-x}S_8$ series hollow spheres. The high-resolution spectra of (b) Co 2p, (c) Ni 2p, and (d) S 2p.

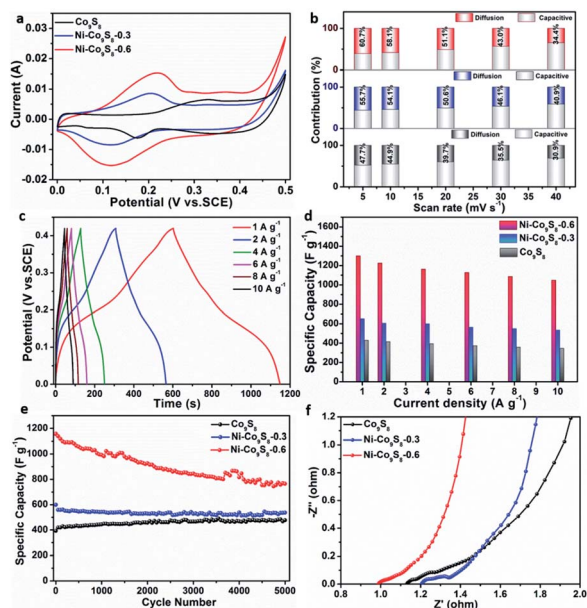Fig. 5 (a) Comparison of CV curves for $Ni_xCo_{9-x}S_8$ series hollow spheres at 5 mV s^{-1}, (b) the diffusion and capacitive-controlled contribution of Co_9S_8 (black), $Ni-Co_9S_8$-0.3 (blue), and $Ni-Co_9S_8$-0.6 (red), (c) GCD of $Ni-Co_9S_8$-0.6, (d) the rate capability of $Ni_xCo_{9-x}S_8$ series electrodes, (e) the cyclic stability at 4 A g^{-1}, and (f) Nyquist plots of $Ni_xCo_{9-x}S_8$ series electrodes.

can effectively increase the specific capacitance and rate capability of pure Co_9S_8 sample. Fig. 5e showed the long-term cyclic performance of the three electrodes at 4 A g^{-1}. The capacity of $Ni-Co_9S_8$-0.6 electrode attenuate to 74.5% after 5000 repeated cycles. More importantly, the mesoporous hollow $Ni-Co_9S_8$-0.6 electrode exhibited a performance comparable to or higher than the recently reported sulfide-related electrodes such as rGO/Co_9S_8 (575.9 F g^{-1}, 2 A g^{-1}),[36] $CoNi_2S_4$/Co_9S_8 composites (1183.3 F g^{-1}, 2 A g^{-1}),[37] Ni_3S_4@Co_9S_8 tubes (1002.2 F g^{-1}, 1 A g^{-1}),[38] CoO/Co_9S_8 hollow microspheres (1100 F g^{-1}, 2 A g^{-1}),[39] GH@NC@Co_9S_8 composite (540 F g^{-1}, 1 A g^{-1}),[40] Co_9S_8 nanowire/Ni (1191.17 F g^{-1}, 2 mV s^{-1}),[41] 0.3 cP/rGO/Co_9S_8 (788.9 F g^{-1}, 1 A g^{-1}),[42] Co_9S_8@N-C@MoS_2 (410 F g^{-1}, 10 A g^{-1}),[43] $Co_3(OH)_2(HPO_4)_2$ @Co_9S_8/Co electrode (1279.4 F g^{-1}, 5 mA cm^{-2}),[44] CoS@NSC-800 (289 F g^{-1}, 1 A g^{-1}),[45] Co_9S_8@$NiCo_2S_4$@NF electrode (1026 F g^{-1}, 1 A g^{-1}),[46] $(Co_{0.94}Fe_{0.06})_9S_8$ hollow spheres (454 F g^{-1}, 1 A g^{-1}),[47] Co_9S_8-2@CN/NF (471.1 F g^{-1}, 0.5 A g^{-1}),[48] Co_9S_8–aCNT–NiCoLDH (1185.5 F g^{-1}, 1 A g^{-1}),[49] and $MnCo_2S_4$/Co_9S_8/Ni composites (1058.0 F g^{-1}, 1 A g^{-1}).[50] A more extensive comparison of super-capacitance performance of $Ni-Co_9S_8$-0.6 with other related electrodes are listed in Table S2.† Furthermore, the improved electrochemical performance of $Ni-Co_9S_8$-0.6 can be supported by the smallest electrolyte resistance (R_s) and charge transfer resistance (R_{ct}) shown in Fig. 5f. The electrolyte resistance of Co_9S_8, $Ni-Co_9S_8$-0.3, and $Ni-Co_9S_8$-0.6 is 1.09, 1.29, and 0.97 Ω, respectively. Furthermore, the charge transfer resistance of Co_9S_8 is 3.39 Ω, which decreased to 1.39 Ω in $Ni-Co_9S_8$-0.6. The straight line with the largest slope in low frequency region also indicated the $Ni-Co_9S_8$-0.6 electrode

exhibit the fast ionic diffusion efficiency and excellent reversibility (Fig. S6†).

Furthermore, a typical $Ni-Co_9S_8$-0.6//Zn alkaline battery is fabricated by using $Ni-Co_9S_8$-0.6 as cathode, Zn plate as anode, and 2 M KOH+0.2 M $Zn(Ac)_2$ as electrolytes. Fig. 6a shows the CV curves of $Ni-Co_9S_8$-0.6//Zn battery at the scan rate of 1–20 mV s^{-1} with the potential range of 1.2–2.0 V vs. Zn. At 1 mV s^{-1}, the $Ni-Co_9S_8$-0.6//Zn displays a pair of redox peaks at 1.8 and 1.65 V. Even the scan rate up to 20 mV s^{-1}, the redox peaks can be preserved, indicated the excellent reversibility of the full battery. The GCD curves obtained at different current densities were shown in Fig. 6b, the GCD curves present a charge and discharge platforms located at 1.774 and 1.675 V at 1 A g^{-1}, with the voltage hysteresis of 0.099 V, demonstrating a less polarization and high energy conversion efficiency at the current density of 1 A g^{-1}. Furthermore, the specific capacitance of the $Ni-Co_9S_8$-0.6//Zn battery decreased from 152 to 97 mA h g^{-1} with its voltage reduced from 1.675 to 1.654 V as the current density increasing from 1 to 10 A g^{-1}. The capacitance retention of 10 A g^{-1} is 64%, indicating the excellent rate performance of $Ni-Co_9S_8$-0.6//Zn battery in alkaline electrolyte. Moreover, when the discharge current density came back to 1 A g^{-1}, the battery can restore the capacitance of 140 mA h g^{-1} (92%), illustrating the tolerance to high speed charge–discharge reaction (Fig. 6c). The maximum charge capacitance approach to the similar aqueous Ni–Zn batteries, such as G-NCGs//Zn battery (113.8 mA h g^{-1}, 0.5 A g^{-1}),[51] Ni_3S_2/Ni//Zn battery (148 mA h g^{-1}, 0.2 A g^{-1}),[52] Zn//$NiCo_2O_4$ (112 mA h g^{-1}, 1 A g^{-1}),[53] Zn//NiO–CNTs battery (155 mA h g^{-1}, 1 A g^{-1}),[54] F-doped Ni–Co hydroxide (FNCH) and oxide constructed FNCH/Ni//Zn battery (88 mA h g^{-1}, 1 A g^{-1}) and FNCO/Ni//Zn battery (159 mA h g^{-1}, 1 A g^{-1}),[55] $ZnCo_2O_{4-x}$//
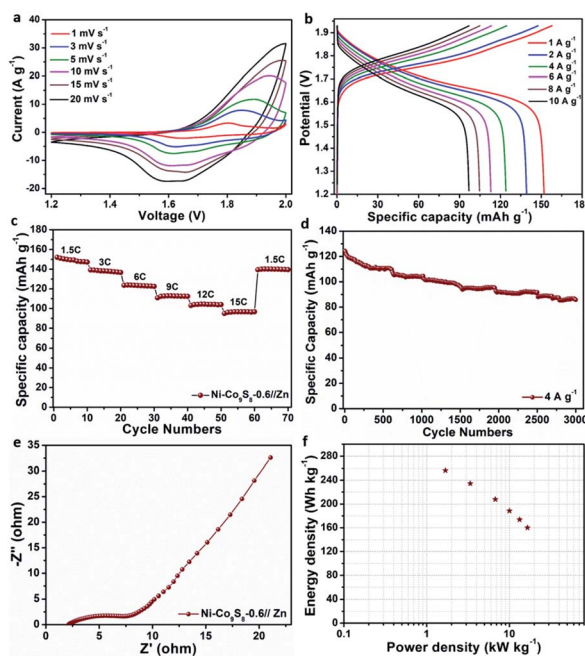

Fig. 6 The electrochemical characterization of $Ni-Co_9S_8$-0.6//Zn battery (a) CV curves, (b) GCD curves, (c) rate capability, (d) the cyclic stability at 4 A g^{-1}, (e) Nyquist plot, and (f) Ragone plot.

Zn (148.3 mA h g^{-1}, 0.05 A g^{-1}),[56] Zn//ZnAl$_{0.67}$Co$_{1.33}$O$_4$ (134 mA h g^{-1}, 16 mA g^{-1}),[57] NiCo$_2$O$_4$-1//Zn (122.5 mA h g^{-1}, 1 A g^{-1}),[58] and NiO/C–Zn (159 mA h g^{-1}, 1 A g^{-1}).[59] Furthermore, the cyclic stability of the Ni-Co$_9$S$_8$-0.6//Zn battery was tested at 4 A g^{-1} for 3000 cycles, the capacity retention kept at 69% (Fig. 6d). The excellent rate capability of Ni-Co$_9$S$_8$-0.6//Zn can be supported by the small charge transfer resistance (Fig. 6e). The power density and energy density of Ni-Co$_9$S$_8$-0.6//Zn battery was calculated and shown in Fig. 6f, the Ni-Co$_9$S$_8$-0.6//Zn battery can achieve the energy density of 256.5 W h kg^{-1} (at 1.69 kW kg^{-1}) and the maximum power density of 16.56 kW kg^{-1} (at 160.1 W h kg^{-1}). The power/energy density of Ni-Co$_9$S$_8$-0.6//Zn battery are comparable with the reported Ni–Zn battery such as β-Ni(OH)$_2$/CNFs//Zn (325 W h kg^{-1} at a power density of 1.23 kW kg^{-1}),[60] Co$_3$O$_4$@NiO NSRAs//Zn (215.51 W h kg^{-1} at 3.45 kW kg^{-1}),[61] Co-Ni$_3$Se$_2$//Zn (199.34 W h kg^{-1}),[62] P-Co$_3$O$_4$//Zn battery (193.7 W h kg^{-1} at 1.6 kW kg^{-1}),[63] N-Fe$_2$O$_{3-x}$//Zn battery (135 W h kg^{-1} at 0.47 kW kg^{-1}),[64] Am-NCS//Zn (254.2 Wh/kg at 3.28 kW kg^{-1}).[65] The excellent performance of Ni-Co$_9$S$_8$-0.6 should be ascribed to the unique mesoporous hollow spheres structure with enriched contact area and highly open structure, which facilities the mass transportation, and the Ni dopant in the Co$_9$S$_8$ matrix can improve the electrical conductivity.

4 Conclusions

In summary, a series of mesoporous hollow Ni$_x$Co$_{9-x}$S$_8$ spheres were synthesized *via* a facile solvothermal method, which exhibit excellent rate capability and long-time cycling performance. Attributed to the improvement of conductivity and abundant active surface, the capacitance of Ni-doped Co$_9$S$_8$ increased dramatically. Remarkably, the optimized Ni-Co$_9$S$_8$-0.6 electrode delivery a capacity of 1300 F g^{-1} at 1 A g^{-1}. Especially, a stable aqueous Ni/Co–Zn battery was constructed by Ni-Co$_9$S$_8$-0.6 as cathode and Zn plate as anode. The Ni-Co$_9$S$_8$-0.6//Zn battery delivers an energy density of 256 W h kg^{-1} and power density of 1.69 kW kg^{-1}. This work provides a facile method to prepare mesoporous hollow structure and cathodes for aqueous Ni–Zn batteries.

Author contributions

Daojun Zhang: methodlogy, writing and editing. Jingchao Zhang: analysis and investigation. Jiaqi Li and Yuting Li, synthesis and characterization. Chenxiang Li and Yingying Liu, software and data curation. Renchun Zhang, editing and review.

Conflicts of interest

There are no conflicts to declare.

Acknowledgements

Notes and references

1 S. X. Sun, J. H. Luo, Y. Qian, Y. Jin, Y. Liu, Y. G. Qiu, X. Li, C. Fang, J. T. Han and Y. H. Huang, *Adv. Energy Mater.*, 2018, **8**, 1801080.

2 J. Pu, Z. H. Wang, K. L. Wu, N. Yu and E. H. Sheng, *Phys. Chem. Chem. Phys.*, 2014, **16**, 785.

3 Y. X. Wen, Y. P. Liu, S. Dang, S. H. Tian, H. Q. Li, Z. L. Wang, D. Y. He, Z. S. Wu, G. Z. Cao and S. L. Peng, *J. Power Sources*, 2019, **423**, 106–114.

4 Y. Q. Zhou, N. Li, L. D. Sun, X. L. Yu, C. Liu, L. Yang, S. D. Zhang and Z. Y. Wang, *Nanoscale*, 2019, **11**, 7457–7464.

5 J. Xu, Q. F. Wang, X. W. Wang, Q. Y. Xiang, B. Liang, D. Chen and G. Z. Shen, *ACS Nano*, 2013, **7**, 5453–5462.

6 N. Zhang, W. C. Wang, C. Q. Teng, Z. X. Wu, Z. R. Ye, M. J. Zhi and Z. L. Hong, *RSC Adv.*, 2018, **8**, 27574–27579.

7 E. S. Goda, A. ur Rehman, B. Pandit, A. Al-Shahat Eissa, S. E. Hong and K. R. Yoon, *Chem. Eng. J.*, 2022, **428**, 132470.

8 X. C. Hou, Y. Z. Zhang, Q. C. Dong, Y. Hong, Y. L. Liu, W. J. Wang, J. J. Shao, W. L. Si and X. C. Dong, *ACS Appl. Energy Mater.*, 2018, **1**, 3513–3520.

9 B. Q. Xie, M. Y. Yu, L. H. Lu, H. Z. Feng, Y. Yang, Y. Chen, H. D. Cui, R. B. Xiao and J. Liu, *Carbon*, 2019, **141**, 134–142.

10 X. Z. Wang, D. C. Su, Y. H. Xiao, S. G. Xu, S. M. Fang and S. K. Cao, *Electrochim. Acta*, 2019, **293**, 419–425.

11 L. L. Li, Y. H. Ding, H. J. Huang, D. S. Yu, S. Y. Zhang, H. Y. Chen, S. Ramakrishna and S. J. Peng, *J. Colloid Interface Sci.*, 2019, **540**, 389–397.

12 L. R. Hou, Y. Y. Shi, S. Q. Zhu, M. Rehan, G. Pang, X. G. Zhang and C. Z. Yuan, *J. Mater. Chem. A*, 2017, **5**, 133–144.

13 Q. Liu, X. D. Hong, X. Zhang, W. Wang, W. X. Guo, X. Y. Liu and M. D. Ye, *Chem. Eng. J.*, 2019, **356**, 985–993.

14 J. X. Zhang, Y. Deng, Y. Q. Wu, Z. Y. Xiao, X. B. Liu, Z. J. Li, R. R. Bu, Q. Zhang, W. Sun and L. Wang, *Chem. Eng. J.*, 2022, **430**, 132836.

15 S. Biswas, V. Sharma, T. Singh and A. Chandra, *J. Mater. Chem. A*, 2021, **9**, 6460–6468.

16 S. Biswas, A. Chowdhury and A. Chandra, *Front. Mater.*, 2019, **6**, 1–11.

17 J. H. Ryu, B. G. Park, S. B. Kim and Y. Park, *J. Appl. Electrochem.*, 2009, **39**, 1059–1066.

18 L. Yin, L. Q. Wang, X. H. Liu, Y. S. Gai, L. H. Su, B. H. Qu and L. Y. Gong, *Eur. J. Inorg. Chem.*, 2015, 2457–2462.

19 L. Wang, S. K. Li, F. Z. Huang, X. Y. Yu, M. J. Liu and H. Zhang, *J. Power Sources*, 2019, **439**, 227103.

20 X. Q. Du, H. Su and X. S. Zhang, *ACS Sustainable Chem. Eng.*, 2019, 7(19), 16917–16926.

21 L. Q. Wu, K. Y. Zhang, T. T. Wang, X. B. Xu, Y. Q. Zhao, Y. Sun, W. Zhong and Y. W. Du, *ACS Appl. Nano Mater.*, 2018, **1**, 1083–1093.

22 S. Biswas, D. Mandal, T. Singh and A. Chandra, *RSC Adv.*, 2021, **11**, 30031–30039.

23 L. Zuniga, V. Agubra, D. Flores, H. Campos, J. Villareal and M. Alcoutlabi, *J. Alloys Compd.*, 2016, **686**, 733–743.

24 S. Biswas, V. Sharma, D. Mandal, A. Chowdhury, M. Chakravarty, S. Priya, C. C. Gowda, P. De, I. Singh and A. Chandra, *CrystEngComm*, 2020, **22**, 1633–1644.

25 X. F. Liu, D. Wang, X. Z. Yang, Z. Z. Zhao, H. Yang, M. Feng, W. Zhang and W. T. Zheng, *ACS Appl. Energy Mater.*, 2019, **2**, 1428–1435.

26 M. M. Yin, X. T. Feng, D. Zhao, Y. Zhao, H. S. Li, W. Zhou, H. B. Liu, X. P. Bai, H. X. Wang, C. H. Feng and Q. Z. Jiao, *ACS Sustainable Chem. Eng.*, 2019, **7**, 6122–6130.

27 H. N. Li, Y. H. Zhang, B. H. Liu, Z. H. Gao, G. F. Zhao, T. T. Liu, X. Gao, S. B. Xia and H. Guo, *Sustainable Energy Fuels*, 2020, **4**, 2208–2219.

28 X. M. Guo, W. Zhang, D. Zhang, S. L. Qian, X. Z. Tong, D. C. Zhou, J. H. Zhang and A. H. Yuan, *ChemElectroChem*, 2019, **6**, 4571–4575.

29 M. Dai and R. Wang, *Small*, 2021, **17**, 2006813.

30 X. Chen, Q. Liu, T. Bai, W. G. Wang, F. L. He and M. D. Ye, *Chem. Eng. J.*, 2021, **409**, 127237.

31 X. R. Hu, Y. Wang, Q. S. Wu and J. F. Li, *Ionics*, 2022, **28**, 989–1015.

32 Y. W. Yu, X. L. Hu, S. Wang, H. D. Qiao, Z. Y. Liu, K. F. Song and X. D. Shen, *Nano Res.*, 2022, **15**, 685–693.

33 X. Y. Gao, J. M. Zhang, W. Yin and X. H. Lu, *NanoSelect*, 2021, **2**, 1642–1660.

34 H. Chen, Z. H. Shen, Z. H. Pan, Z. K. Kou, X. M. Liu, H. Zhang, Q. L. Gu, C. Guan and J. Wang, *Adv. Sci.*, 2019, **6**, 1802002.

35 J. Pu, T. T. Wang, H. Y. Wang, Y. Tong, C. C. Lu, W. Kong and Z. H. Wang, *ChemPlusChem*, 2014, **79**, 577–583.

36 P. Wang, C. Y. Li, W. G. Wang, J. Wang, Y. S. Zhu and Y. P. Wu, *Chin. Chem. Lett.*, 2018, **29**, 612–615.

37 F. L. Zhao, W. X. Huang, H. T. Zhang and D. M. Zhou, *Appl. Surf. Sci.*, 2017, **426**, 1206–1212.

38 H. Li, F. Yue, H. T. Xie, C. Yang, Y. Zhang, L. G. Zhang and J. D. Wang, *CrystEngComm*, 2018, **20**, 889–895.

39 Y. P. Wang, T. Zhu, Y. F. Zhang, X. Z. Kong, S. Q. Liang, G. Z. Cao and A. Q. Pan, *J. Mater. Chem. A*, 2017, **5**, 18448–18456.

40 H. T. Niu, Y. Zhang, Y. Liu, B. F. Luo, N. Xin and W. D. Shi, *J. Mater. Chem. A*, 2019, **7**, 8503–8509.

41 S. J. Patil, A. C. Lokhande, J. S. Park, J. H. Kim, Y. B. Kim, B. C. Choi, S. H. Park, S. H. Jung and D. W. Lee, *J. Ind. Eng. Chem.*, 2018, **61**, 206–215.

42 T. H. Yao, Y. L. Li, D. Q. Liu, Y. P. Gu, S. C. Qin, X. Guo, H. Guo, Y. Q. Ding, Q. M. Liu, Q. Chen, J. S. Li and D. Y. He, *J. Power Sources*, 2018, **379**, 167–173.

43 X. C. Hou, Y. Z. Zhang, Q. C. Dong, Y. Hong, Y. L. Liu, W. J. Wang, J. J. Shao, W. L. Si and X. C. Dong, *ACS Appl. Energy Mater.*, 2018, **1**, 3513–3520.

44 Z. Q. Zhu, J. H. Lin, N. Li, R. Z. Zhang, K. F. Zhang, C. H. Zhao, G. R. Chen and C. J. Zhao, *J. Phys. Chem. C*, 2020, **124**, 83–91.

45 Z. Xiao, G. Z. Xiao, M. H. Shi and Y. Zhu, *ACS Appl. Mater. Interfaces*, 2018, **10**, 16436–16448.

46 Y. Y. Yang, D. L. Qian, H. Zhu, Q. Zhou, Z. Y. Zhang, Z. M. Li and Z. A. Hu, *J. Alloys Compd.*, 2022, **898**, 162850.

47 Y. N. Wang, Z. S. Meng, X. L. Gong, C. Jiang, C. X. Zhang, J. Xu, Y. X. Li, J. Y. Bao, Y. N. Cui, H. B. Wang, Y. Zeng, X. Y. Hu, S. S. Yu and H. W. Tian, *Chem. Eng. J.*, 2022, **431**, 133980.

48 Z. Wang, M. L. Wang, K. He, X. X. Hang and Y. F. Bi, *Chem.–Asian J.*, 2021, **16**, 1486–1492.

49 C. Sun, L. Sun, K. F. Fan, Y. Shi, J. L. Gu, Y. F. Lin, J. J. Hu and Y. H. Zhang, *Dalton Trans.*, 2021, **50**, 9283–9292.

50 X. Wei, H. Y. Wu and L. L. Li, *J. Taiwan Inst. Chem. Eng.*, 2020, **111**, 198–204.

51 X. Y. Zhang, J. J. He, L. J. Zhou, H. Z. Zhang, Q. S. Wang, B. B. Huang, X. H. Lu, Y. X. Tong and C. S. Wang, *Adv. Funct. Mater.*, 2021, **31**, 2100443.

52 P. Hu, T. S. Wang, J. W. Zhao, C. J. Zhang, J. Ma, H. P. Du, X. G. Wang and G. L. Cui, *ACS Appl. Mater. Interfaces*, 2015, **7**, 26396–26399.

53 J. Wang, Z. J. Jia, S. B. Li, Y. Wang, W. Guo and T. Qi, *Bull. Mater. Sci.*, 2015, **38**, 1435.

54 X. W. Wang, M. X. Li, Y. F. Wang, B. W. Chen, Y. S. Zhu and Y. P. Wu, *J. Mater. Chem. A*, 2015, **3**, 8280–8283.

55 W. Liu, Y. J. Chen, Y. Y. Wang, Q. W. Zhao, L. B. Chen, W. F. Wei and J. M. Ma, *Energy Storage Mater.*, 2021, **37**, 336–344.

56 J. J. Huang, Y. Y. Li, R. K. Xie, J. W. Li, Z. H. Tian, G. L. Chai, Y. W. Zhang, F. L. Lai, G. J. He, C. T. Liu, T. X. Liu and D. J. L. Brett, *J. Energy Chem.*, 2021, **58**, 147–155.

57 C. S. Pan, R. G. Nuzzo and A. A. Gewirth, *Chem. Mater.*, 2017, **29**, 9351–9359.

58 H. L. Du, J. H. Lei, K. X. Xiang, W. J. Lin, J. C. Zheng and H. Y. Liao, *J. Alloys Compd.*, 2021, **896**, 162925.

59 J. L. Li and C. G. Chen, *J. Porous Mater.*, 2020, **27**, 1447–1454.

60 Y. Jian, D. M. Wang, M. Z. Huang, H. L. Jia, J. H. Sun, X. K. Song and M. Y. Guan, *ACS Sustainable Chem. Eng.*, 2017, **5**, 6827–6834.

61 Z. Y. Lu, X. C. Wu, X. D. Lei, Y. P. Li and X. M. Sun, *Inorg. Chem. Front.*, 2015, **2**, 184–187.

62 D. A. Reddy, H. Lee, M. Gopannagari, D. P. Kumar, K. Kwon, H. D. Yoo and T. K. Kim, *Int. J. Hydrogen Energy*, 2020, **45**, 7741–7750.

63 F. Yang, K. Zhang, Z. Cen and K. B. Xu, *J. Alloys Compd.*, 2021, **879**, 160439.

64 C. L. Teng, C. Q. Zhang, K. S. Yin, M. X. Zhao, Y. S. Du, Q. Wu and X. H. Lu, *Sci. China Mater.*, 2022, **65**, 920–928.

65 N. Li, G. M. Qu, X. X. Zhang, S. S. Zhao, C. G. Wang, G. Zhao, P. Y. Hou and X. J. Xu, *Chin. Chem. Lett.*, 2022, **33**, 3272–3276.